Article

Weak upper-mantle base revealed by postseismic deformation of a deep earthquake

https://doi.org/10.1038/s41586-022-05689-8

Received: 24 March 2022

Accepted: 28 December 2022

Published online: 22 February 2023

Check for updates

Sunyoung Park[1]✉, Jean-Philippe Avouac[2], Zhongwen Zhan[2] & Adriano Gualandi[3]

Mantle viscosity plays a key role in the Earth's internal dynamics and thermal history. Geophysical inferences of the viscosity structure, however, have shown large variability depending on the types of observables used or the assumptions imposed[1–3]. Here, we study the mantle viscosity structure by using the postseismic deformation following a deep (approximately 560 km) earthquake located near the bottom of the upper mantle. We apply independent component analysis[4] to geodetic time series to successfully detect and extract the postseismic deformation induced by the moment magnitude 8.2, 2018 Fiji earthquake. To search for the viscosity structure that can explain the detected signal, we perform forward viscoelastic relaxation modelling[5,6] with a range of viscosity structures. We find that our observation requires a relatively thin (approximately 100 km), low-viscosity (10^{17} to 10^{18} Pa s) layer at the bottom of the mantle transition zone. Such a weak zone could explain the slab flattening[7] and orphaning[8] observed in numerous subduction zones, which are otherwise challenging to explain in the whole mantle convection regime. The low-viscosity layer may result from superplasticity[9] induced by the postspinel transition, weak $CaSiO_3$ perovskite[10], high water content[11] or dehydration melting[12].

Mantle rheology governs the pattern and rate of mantle convection—the mixing and recycling of materials, descending of subducting slabs and upwelling of plumes—and the Earth's thermal evolution. Despite its importance, the rheological structure of the mantle remains poorly understood. Besides the strong lithosphere and the overall increase in viscosity from the upper to lower mantle, existing radial viscosity models[1–3] exhibit remarkable variability. These models usually include weak layers, but their locations and thicknesses differ considerably. Some have a weak asthenosphere, whereas others have a weak layer at a deeper depth, generally around the mantle transition zone (MTZ). The existence of a low-viscosity layer between the upper and lower mantle has been inferred in studies of the long-wavelength geoid and glacial isostatic adjustment[3,13] despite large variations in the exact depth and thickness of the layer. On the other hand, it has been pointed out that a weak layer in the MTZ might not be consistent with the geoid highs associated with subducting slabs[14]. Therefore, adding a completely independent type of observable would be consequential in improving our understanding of the Earth's viscosity structure.

In this article, we study the deep viscosity structure by examining the Earth's response to a deep earthquake. Even though the principle of using postseismic observations to constrain viscosity has long been used (for example, in ref. [15]), it has not yet been applied to deep earthquakes owing to the difficulty of extracting their postseismic signal. Some recent observations[16], however, suggests that it might be possible. Here we examine the postseismic deformation following the approximately 560-km deep moment magnitude (M_w) 8.2 Fiji earthquake, one of the largest deep events ever recorded (Fig. 1a). The event occurred on August 19, 2018 in the Tonga subduction zone, where the Pacific Plate is subducting westward under the Tonga trench. Even though the epicentre is located in the middle of the Southern Pacific Ocean, there are numerous islands including Fiji and New Caledonia with available Global Navigation Satellite System (GNSS) data. The list of the 35 GNSS stations used in this study can be found in Extended Data Table 1.

To make robust detection of the postseismic deformation following such a deep earthquake at the Earth's surface, we use an advanced data processing technique based on independent component analysis (ICA), which has been tailored to the analysis of postseismic geodetic time series[4]. Our approach allows the extraction of the postseismic signal without any a priori assumption about its time evolution and allows us to distinguish the signal from others including the seasonal deformation and reference frame jitter (Methods). By applying this technique to the three-component (east, north and vertical) GNSS position time series of the time period from January 2017 to July 2020, centred around the event time, we successfully detect the postseismic deformation (Fig. 1).

The spatial extent of the observed deformation reaches as far as about 2,000 km from the epicentre, whereas most of the significant displacements are located within 1,000 km. Horizontal displacements up to approximately 8 mm and vertical displacements up to approximately

[1]Department of the Geophysical Sciences, The University of Chicago, Chicago, IL, USA. [2]Division of Geological and Planetary Sciences, California Institute of Technology, Pasadena, CA, USA. [3]Istituto Nazionale di Geofisica e Vulcanologia, Rome, Italy. ✉e-mail: sunnypark@uchicago.edu

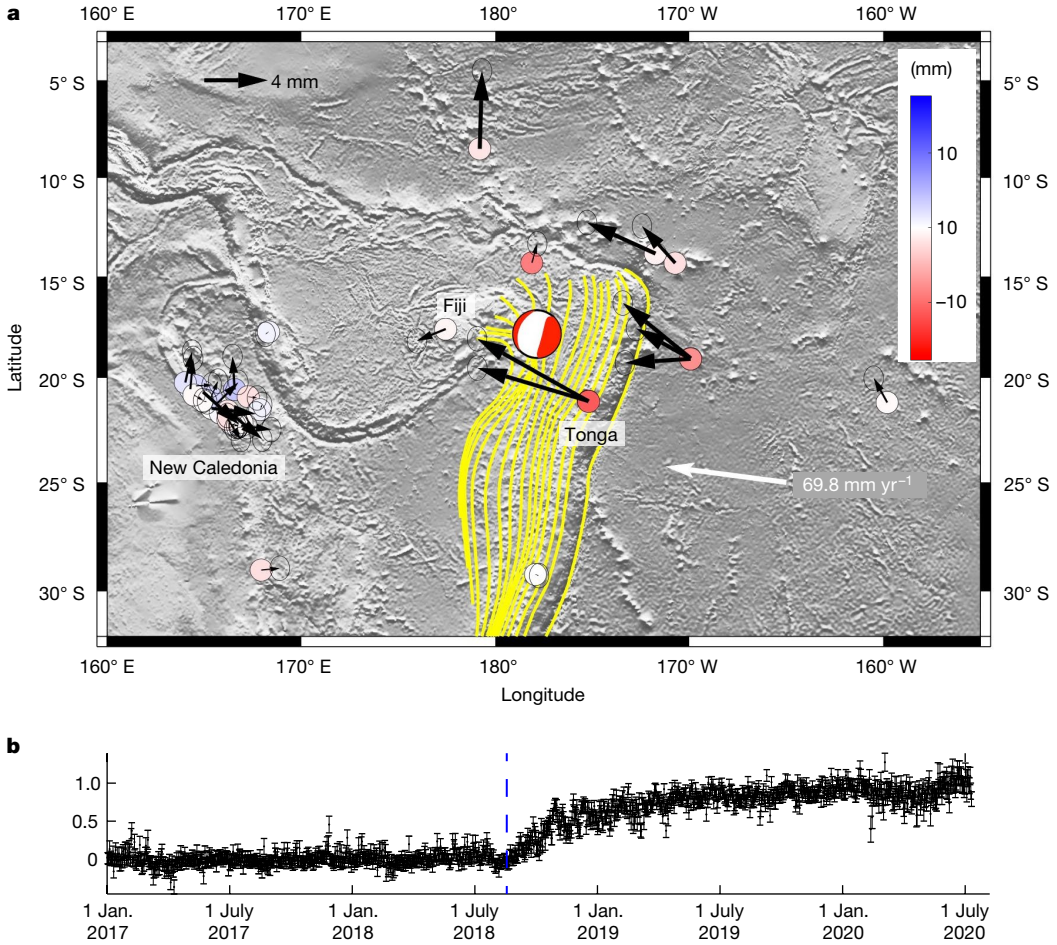

Fig. 1 | Postseismic deformation detected following the 560-km deep M_w 8.2 Fiji earthquake. a, The red and white circle shows the centroid moment tensor. The other coloured circles show the GNSS stations, colour-coded to represent uplift (blue) or subsidence (red), measured approximately 2 years after the earthquake (the standard deviation on the vertical displacement is 1.53 mm (Methods)). The black arrows and black open ellipses represent the horizontal displacements and their uncertainties (GNSS stations that are close to each other result in multiple arrows with similar origins). The background shows bathymetry[26] with slab contours[27] (yellow lines). The white arrow shows the Pacific plate velocity with respect to the Australian plate. **b**, Time evolution of the extracted postseismic deformation shown with one standard deviation error bars, normalized to a unit amplitude. The blue dashed line shows the time of the earthquake.

17 mm are detected, with the largest displacements found at the stations in the Tonga islands located at about 460 km southeast of the epicentre. Most stations within 1,000 km from the epicentre show westward to northward motion and subsidence. In New Caledonia the signal is faint, but most stations exhibit uplift rather than subsidence. Such spatial coherence of the extracted signal, that is, large displacements close to the earthquake and comparable displacements in neighbouring stations, confirms the robustness of the detection, considering that the ICA ignores the information about the station locations and treats each time series equally. The time evolution of the extracted signal also corroborates the robust detection of the postseismic deformation: the deformation starts abruptly at the time of the earthquake and the deformation rate decays gradually over time, as is commonly observed for shallow earthquakes.

We find that the observed postseismic deformation requires a viscoelastic relaxation mechanism. The postseismic displacements show a spatial pattern clearly distinct from the coseismic displacements (Extended Data Fig. 1 and Methods), excluding the fact that it would reflect afterslip[17] around the earthquake source. Considering the large depth of the Fiji earthquake compared to the spatial extent of the source, afterslip would indeed produce surface displacements that are approximately proportional to the coseismic displacements, and thus, would result in a similar spatial pattern. However, station LAUT, for example, shows large coseismic displacements, but relatively small postseismic displacements compared to other GNSS stations. Moreover, the fact that the postseismic deformation takes place throughout a broader area while having smaller absolute amplitudes than the coseismic deformation, that is, not proportional to the coseismic deformation, points to postseismic deformation caused by viscoelastic relaxation. The broadness of the postseismic deformation and their significant amplitudes, that is, reaching close to a half or a third of those of the coseismic displacements within less than 2 years, suggests the presence of a low-viscosity structure with a short Maxwell time. We have also investigated the potential effect of the M_w 7.9 aftershock, which occurred 18 days later at depth approximately 100 km deeper than the mainshock[18]. We found that even the coseismic displacements from the aftershock are too small to be detected, suggesting that the postseismic deformation from the aftershock should be negligible as well.

To investigate a viscosity structure that can best explain our observations, we perform numerical modelling of the postseismic viscoelastic relaxation process[5,6] (Methods). We first gain insights by exploring a broad range of viscosity structures: cases with or without a low-viscosity layer, and cases with or without the subducting slab. The model without any zone of low viscosity (Fig. 2a) cannot produce any significant surface deformation, demonstrating that a weak zone is essential. We also test the effect of the subducting slab by removing it (Fig. 2b).

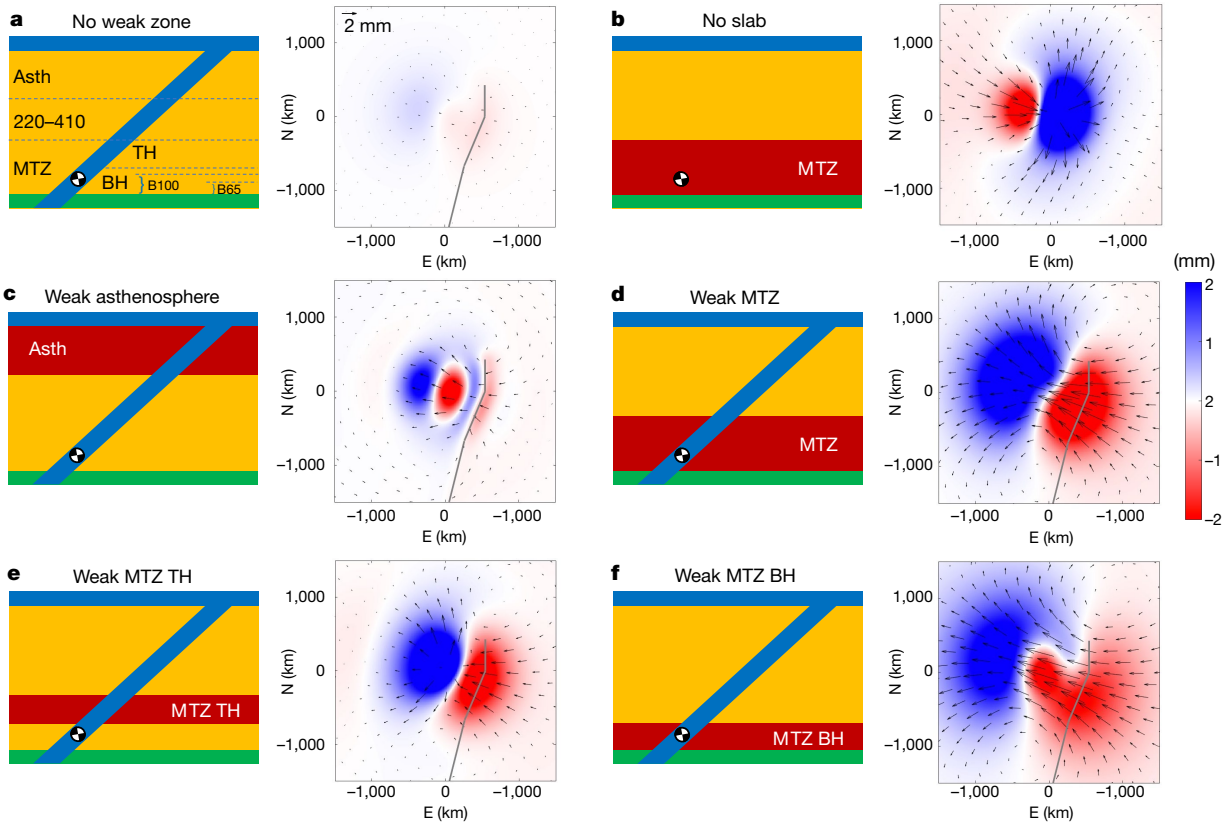

Fig. 2 | Predicted postseismic deformation following the M_w 8.2 Fiji event for different viscosity structures. a, Structure without any weak zone shown with the elastic lithosphere and slab in blue and the upper and lower mantle in yellow and green, respectively. The black and white circle shows the centroid location. The upper mantle is divided by dashed lines to show asthenosphere (Asth), mantle transition zone (MTZ) and 220–410 (the zone between the Asth and MTZ; depths from 220 to 410 km). The MTZ is subdivided into MTZ TH, MTZ BH, MTZ B100 and MTZ B65 (left). Horizontal (black arrows) and vertical (blue, uplift; red, subsidence) components of the postseismic displacement predicted up to the last observation (approximately year 2020.5, Fig. 1) corresponding to the structure shown on the left are plotted within ±1,500 km east (E) and north (N) of the centroid location. The grey line shows the trench locations of the input slab model (right). **b**, The same as **a**, but with a weak MTZ (Maxwell time of 1.25 years) and no slab. **c**, The same as **a**, but with a weak asthenosphere (Maxwell time of 1.25 years). **d**, The same as **a**, but with a weak MTZ (Maxwell time of 1.25 years). **e**, The same as **a**, but with a weak MTZ TH (Maxwell time of 0.63 years). **f**, The same as **a**, but with a weak MTZ BH (Maxwell time of 0.63 years). This model fits the data the best among the six models.

Both the horizontal and vertical displacements are close to being in the precise opposite direction to those of the cases with the slab present (for example, Fig. 2d), and are irreconcilable with the observation (Fig. 1a). Even though one might expect that the deformation pattern would be largely affected by the weak zones, particularly in the first few years after the earthquake, our result shows that the effect of strong structures like the slab is remarkable. This is probably because the slab mechanically connects the deep source and the Earth's surface directly. Given that one-dimensional (1D) modelling, that is, modelling with a depth-dependent structure, cannot capture such a slab structure, our results show the necessity of three-dimensional (3D) modelling for studying postseismic deformation following deep earthquakes.

Recognizing that the observation requires a low-viscosity zone and the subducting slab, we include both elements in further modelling experiments. With the slab structure fixed, different locations of the weak layer are examined, including the asthenosphere and MTZ. We find that the modelling results from a weak asthenosphere (Fig. 2c) and weak MTZ (Fig. 2d) are considerably different in their spatial patterns. Although the deformation is more focused in the vicinity of the earthquake in the case of the weak asthenosphere, the weak MTZ case shows a relatively broad field of deformation with the maximum deformation taking place close to the trench rather than the epicentre. In contrast to the vertical displacement field predicted in the weak MTZ case that exhibits a simple divide between zones of uplift and subsidence, the weak asthenosphere results in a more complex pattern. The effect of the slab structure is also evident in the case of the weak asthenosphere in that the sign of the vertical displacement changes across the trench, which does not occur without the slab. We find that having the weak zone at the MTZ better matches the spatial pattern of the observation in general, with pronounced displacements near the trench, for example, in the Tonga islands.

Considering that the weak MTZ is preferred, we further investigate whether having weak zones at different locations within the MTZ has a significant effect on the surface deformation. We perform additional modelling with thinner weak zones: the top and bottom half of the MTZ, that is, MTZ TH and MTZ BH (Fig. 2e,f). Viscosity that is twice as low as that of the weak MTZ case is used such that the amplitudes of the deformation become comparable. The two modelling results are distinct from each other. The weak MTZ TH case exhibits uplift near the earthquake location, and the overall pattern is in between the weak MTZ and weak asthenosphere cases. In contrast, the predicted deformation for the weak MTZ BH case has the domain of subsidence bulging out to the centre and a relatively broad area of deformation. These results illustrate that the postseismic deformation is highly sensitive to the location and thickness of the weak zone.

In addition to the location of the low-viscosity zone, we also explore different viscosities of the weak zones. We consider viscosities of about 6.1×10^{18} Pa s and lower, that is, a Maxwell time of 2.5 years and shorter, which are more than one and two orders of magnitude lower than those of the upper and lower mantle, respectively. For each viscosity

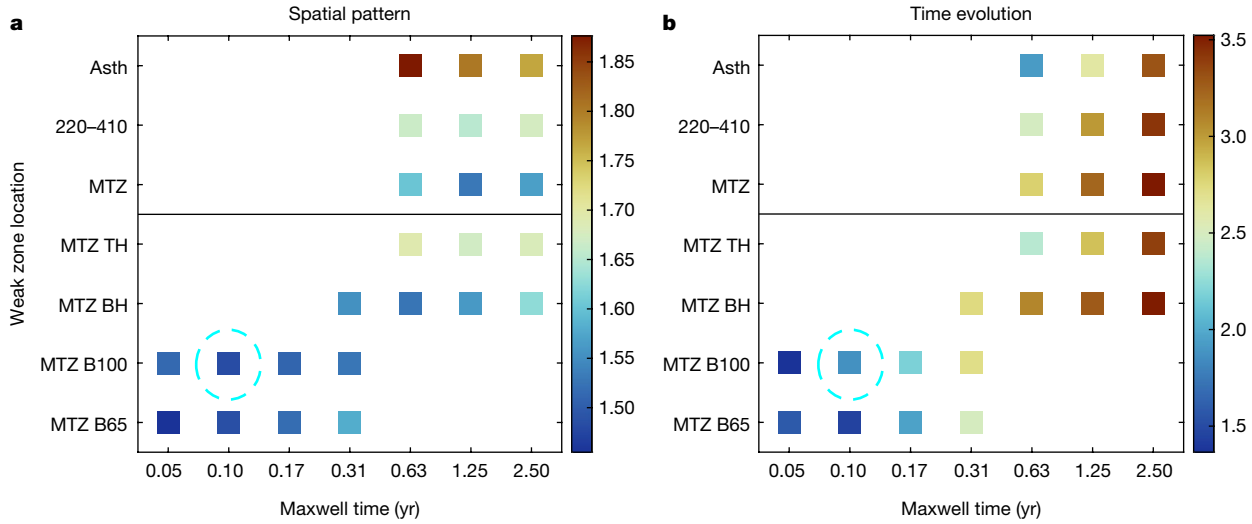

Fig. 3 | Search for the viscosity models that best explain the observation. **a**, Misfits to the GNSS displacements for different weak zone locations (vertical axis) as shown in the left panel of Fig. 2a, with various Maxwell times (horizontal axis). The cyan dashed circle shows the preferred model (inset in Fig. 4a). **b**, The same as **a**, except the misfits are for the time evolution. Note that the thicker the weak zone, the longer the best-fitting Maxwell time (as shown in **a**), but a long Maxwell time (greater than 1 yr) cannot explain the time evolution; fitting the data in time and space, therefore, points to a thin weak zone.

structure, we find that decreasing the viscosity of the weak zone by half leads to about a twofold increase in the amplitudes of the surface displacements while causing little change in the directions (Extended Data Fig. 2). Lowering the viscosity also alters the time evolution of the deformation such that the deformation is more rapid initially, as expected from the shorter Maxwell time (Extended Data Fig. 3b,d).

To find the desirable combination of the weak zone location and its viscosity, we evaluate the fit to the observed 3-component displacements (Fig. 3a and Methods). We examine models with five different locations of the weak zone—'Asth' (the asthenosphere), '220–410' (the zone between the Asth and the MTZ with depths from 220 to 410 km), MTZ, 'MTZ TH' (MTZ top half) and 'MTZ BH' (MTZ bottom half)—

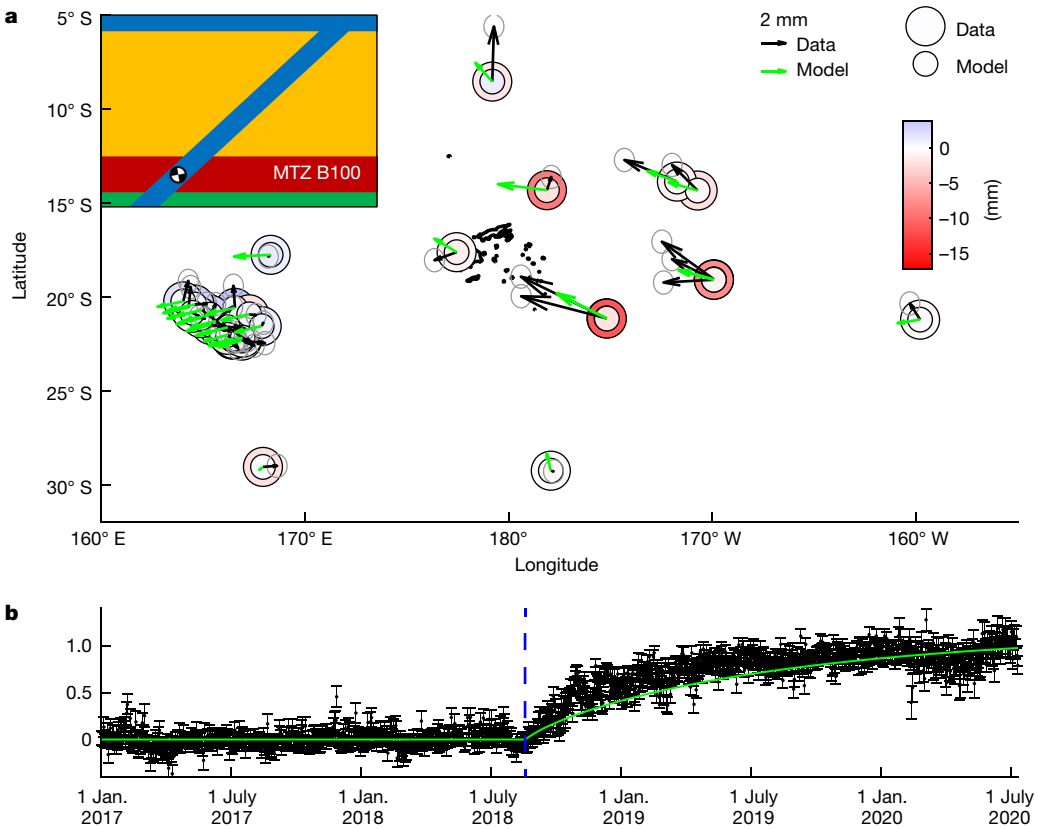

Fig. 4 | Postseismic deformation predicted by our preferred model (MTZ B100 with 0.1 year Maxwell time) compared against the data. **a**,**b**, Postseismic deformation shown in the same manner as in Fig. 1a,b, for the data (black arrows, grey error ellipses and large circles in **a**, and error bars in **b**) and our preferred model (green arrows and small circles in **a**, and green line in **b**). The inset in **a** shows our preferred model, corresponding to the cyan dashed circles in Fig. 3.

and with the Maxwell time from 0.63 to 2.5 years. A deeper weak zone is clearly preferred. Among these models, the best-fitting model is the weak MTZ BH with a Maxwell time of 0.63 years (Extended Data Fig. 3a,b). Lowering the viscosity or shortening the Maxwell time (for example, to 0.31 years) of the MTZ BH does not improve the fit. The second-best model is the MTZ with 1.25 years of Maxwell time. The weak MTZ models fit the data significantly better than the weak MTZ TH models, indicating that having the weak zone at the MTZ BH is crucial to explaining the data.

Considering that the weak zone close to the base of the MTZ is preferred, we examine two additional weak zone locations: 'MTZ B100' (the bottom 100 km of the MTZ) and 'MTZ B65' (the bottom 65 km of the MTZ). The MTZ B65 is twice as thin as the MTZ BH, and the MTZ B100 is in between. Given the reduced thickness, we explore relatively low ranges of viscosities that can produce significant surface deformation, corresponding to the Maxwell time of 0.05 to 0.31 years. We find that these relatively thin weak zones with the Maxwell time of 0.05 or 0.1 years fit the data considerably better than the weak MTZ BH case, not only for the displacements but also for the time evolution of the deformation (Figs. 3 and 4 and Extended Data Fig. 3). Note that the good fit to the time evolution (Fig. 3b) is not meaningful if the fit to the displacements (Fig. 3a) is poor.

Among these models of thin weak zones, our preferred model is the MTZ B100 with 0.1 years of Maxwell time, that is, about 3.8×10^{17} Pa s of viscosity, which results in a good fit to the spatial pattern (see Methods for the conversion between the Maxwell time and the viscosity). Even though the MTZ B65 model with 0.05 years of Maxwell time fits the data well, we find that this model does not predict large enough surface displacements in general (Extended Data Fig. 3c and see Methods for details). Our preferred model, on the other hand, can explain not only the directions and amplitudes of the postseismic displacements in all three components, but also the time evolution of the deformation (Fig. 4). In some cases, misfits in the displacements are significant compared to the observational uncertainties such as in the horizontal component of station FTNA, located at the north of the epicentre. These misfits are probably caused by the heterogeneous elastic structure, which is not accounted for in our modelling. We observe the effect of the heterogeneous elastic structure from the misfit between the observed coseismic displacements and the predicted displacements by using a homogeneous elastic structure. Therefore, we expect a similar effect to be present for the postseismic displacements. It is possible that 3D viscosity structures, other than the slab, might have some effect. We, therefore, have tested several cases by including a weak mantle wedge and a Samoan plume, but these have not resulted in a better fit to the data. It should also be noted that our results require the weak zone at the bottom of the MTZ, but do not exclude the existence of a weak asthenosphere[19,20], as shown by additional tests (Extended Data Fig. 4). This is because postseismic displacements are dominated by the deformation of the deeper layer where the coseismic stress is larger; the signal from the weak asthenosphere is smaller and overprinted. The additional tests actually indicate that if a weak asthenosphere is included, a thin low-viscosity zone at the base of the MTZ is even more strongly required. We can also exclude the possibility that the whole upper mantle has a low short-term viscosity. A low viscosity consistent with the short Maxwell time derived from the observation, if assigned to the whole upper mantle, would yield surface displacements that are too large.

The thin weak layer at the bottom of the MTZ inferred based on the postseismic deformation is consistent with a subset of viscosity profiles proposed by previous studies that used other geophysical observables (for example, refs. [13,21]). The viscosity of 3.8×10^{17} Pa s (approximately 400 times less viscous than the upper mantle) from our preferred model is 2.5 or 20 times less than those from previous studies, but such a discrepancy is expected if the mantle rheology is bi-viscous or non-linear as is generally admitted; in other words, it is possible that (1) the postseismic deformation is a relatively short-term transient process, essentially informing us about the transient viscosity rather than the long-term viscosity in the case of a Burger's bi-viscous rheology[22], and (2) the response to the high stress perturbation caused by a nearby earthquake results in an apparent low effective viscosity in the case of a non-linear rheology. One can also expect that frequent occurrences of deep earthquakes would result in an extra-low effective viscosity locally due to the coseismic stress variations. It is, thus, probable that a low long-term viscosity, which controls the long-term deformation processes, is manifested as a lower transient viscosity. We also note that the presence of the weak layer at the bottom of the MTZ is strongly supported regardless of the absolute viscosity. This is because the effects of the location and the viscosity of the weak zone on the postseismic deformation are largely decoupled; the location of the weak layer has major control over the spatial pattern of the surface displacements (Fig. 3a), whereas the viscosity of the weak layer mainly changes the overall amplitude and the time evolution of the displacements (Fig. 3b).

The detection of a weak layer at the bottom of the MTZ is consequential to the understanding of mantle dynamics. Such a narrow zone of a weak layer can explain the stagnation and flattening of the subducting slab[7] and orphaning of the slab[8], observations that are otherwise challenging to understand within the whole mantle convection regime. In fact, the Tonga subduction zone examined in this study exhibits both flattening and orphaning of the slab[8,23]. There are several subduction systems with stagnant or orphaning behaviours of slabs, which may be the manifestation of the globally distributed low-viscosity layer between the upper and the lower mantle. Note that the flat part of the Tonga slab is mostly below the upper mantle, but our modelling considers a slab geometry that penetrates straight through the lower mantle. However, the slab geometry below the weak zone, or the high-viscosity structure below the weak zone, have little effect on the modelling results based on our test.

There are a few potential mechanisms that can be responsible for the low-viscosity layer. These include the superplasticity associated with the postspinel phase transition[9], weak $CaSiO_3$ perovskite[10], the MTZ with a high water content[11,24] (particularly for Ringwoodite)[25] or dehydration melting[12] under wet mantle conditions. These mechanisms involve common mineral phases or their transformations, and thus would support the weak layer as a global feature that could be enhanced locally where deep earthquakes are frequent.

Online content

Any methods, additional references, Nature Portfolio reporting summaries, source data, extended data, supplementary information, acknowledgements, peer review information; details of author contributions and competing interests; and statements of data and code availability are available at https://doi.org/10.1038/s41586-022-05689-8.

1. Karato, S.Rheology of the Earth's mantle: a historical review. *Gondwana Res.* **18**, 17–45 (2010).
2. King, S. D. Reconciling laboratory and observational models of mantle rheology in geodynamic modelling. *J. Geodyn.* **100**, 33–50 (2016).
3. Rudolph, M. L., Lekić, V. & Lithgow-Bertelloni, C. Viscosity jump in Earth's mid-mantle. *Science.* **350**, 1349–1352 (2015).
4. Gualandi, A., Serpelloni, E. & Belardinelli, M. E. Blind source separation problem in GPS time series. *J. Geod.* **90**, 323–341 (2016).
5. Barbot, S. & Fialko, Y. A unified continuum representation of post-seismic relaxation mechanisms: semi-analytic models of afterslip, poroelastic rebound and viscoelastic flow. *Geophys. J. Int.* **182**, 1124–1140 (2010).
6. Barbot, S. & Fialko, Y. Fourier-domain Green's function for an elastic semi-infinite solid under gravity, with applications to earthquake and volcano deformation. *Geophys. J. Int.* **182**, 568–582 (2010).
7. Mao, W. & Zhong, S. Slab stagnation due to a reduced viscosity layer beneath the mantle transition zone. *Nat. Geosci.* **11**, 876–881 (2018).
8. Grima, A. G., Lithgow-Bertelloni, C. & Crameri, F. Orphaning regimes: the missing link between flattened and penetrating slab morphologies. *Front. Earth Sci.* **8**, 1–19 (2020).
9. Panasyuk, S. V. & Hager, B. H. A model of transformational superplasticity in the upper mantle. *Geophys. J. Int.* **133**, 741–755 (1998).

10. Immoor, J. et al. Weak cubic CaSiO3 perovskite in the Earth's mantle. *Nature* **603**, 276–279 (2022).
11. Fei, H. et al. A nearly water-saturated mantle transition zone inferred from mineral viscosity. *Sci. Adv.* **3**, e1603024 (2017).
12. Schmandt, B., Jacobsen, S. D., Becker, T. W., Liu, Z. & Dueker, K. G. Dehydration melting at the top of the lower mantle. *Science.* **344**, 1265–1268 (2014).
13. Mitrovica, J. X. & Forte, A. M. A new inference of mantle viscosity based upon joint inversion of convection and glacial isostatic adjustment data. *Earth Planet. Sci. Lett.* **225**, 177–189 (2004).
14. Liu, H., Gurnis, M. & Leng, W. Constraints on mantle viscosity from slab dynamics. *J. Geophys. Res. Solid Earth* **126**, 1–18 (2021).
15. Pollitz, F. F. Gravitational viscoelastic postseismic relaxation on a layered spherical Earth. *J. Geophys. Res. Solid Earth* **102**, 17921–17941 (1997).
16. Xu, C., Su, X., Liu, T. & Sun, W. Geodetic observations of the co- and post-seismic deformation of the 2013 Okhotsk Sea deep-focus earthquake. *Geophys. J. Int.* **209**, 1924–1933 (2017).
17. Avouac, J.-P. From geodetic imaging of seismic and aseismic fault slip to dynamic modeling of the seismic cycle. *Annu. Rev. Earth Planet. Sci.* **43**, 233–271 (2015).
18. Jia, Z. et al. The 2018 Fiji Mw 8.2 and 7.9 deep earthquakes: one doublet in two slabs. *Earth Planet. Sci. Lett.* **531**, 115997 (2020).
19. Han, S., Sauber, J. & Pollitz, F. Postseismic gravity change after the 2006–2007 great earthquake doublet and constraints on the asthenosphere structure in the central Kuril Islands. *Geophys. Res. Lett.* **43**, 3169–3177 (2016).
20. Tian, Z., Freymueller, J.T. & Yang, Z. Postseismic deformation due to the 2012 M w 7.8 Haida Gwaii and 2013 M w 7.5 Craig earthquakes and its implications for regional rheological structure.*J. Geophys. Res. Solid Earth* **126**, (2021).
21. Forte, A. M., Dziewonski, A. M. & Woodward, R. L. in *Dynamics of Earth's Deep Interior and Earth Rotation* (eds. Le Mouël, -L. et al.) 135–166 (1993).
22. Lau, H. C. P. & Holtzman, B. K. "Measures of dissipation in viscoelastic media" extended: toward continuous characterization across very broad geophysical time scales. *Geophys. Res. Lett.* **46**, 9544–9553 (2019).
23. van der Hilst, R. Complex morphology of subducted lithosphere in the mantle beneath the Tonga trench. *Nature* **374**, 154–157 (1995).
24. Huang, X., Xu, Y. & Karato, S. Water content in the transition zone from electrical conductivity of wadsleyite and ringwoodite. *Nature* **434**, 746–749 (2005).
25. Pearson, D. G. et al. Hydrous mantle transition zone indicated by ringwoodite included within diamond. *Nature* **507**, 221–224 (2014).
26. NOAA National Geophysical Data Center. 2-minute Gridded Global Relief Data (ETOPO2) v2. NOAA National Centers for Environmental Information. https://doi.org/10.7289/V5J1012Q (2006).
27. Hayes, G. P., Wald, D. J. & Johnson, R. L. Slab1.0: a three-dimensional model of global subduction zone geometries. *J. Geophys. Res.* **117**, B01302 (2012).

Methods

Data selection and preprocessing

We consider GNSS stations within 2,000 km with respect to the epicentre (latitude = 18.113° W, longitude = 178.153° S). Among them, we select ones that have time series data of at least 40% within the studied time period, and this results in the 35 stations listed in Extended Data Table 1.

For each GNSS time series, we first remove the linear trend associated with the long-term plate motions estimated by the median interannual difference adjusted for skewness (MIDAS)[28]. We then remove steps associated with instrumental issues and coseismic signals from the Fiji and other earthquakes, and postseismic signals from other significant shallow earthquakes if there are any (Extended Data Fig. 5). The steps and transients are estimated by finding the best-fitting trajectory model that includes the MIDAS velocities, steps, transients and annual and semiannual sinusoids. For station TONG, which does not have MIDAS velocity estimates, we use the linear trend estimated by the Jet Propulsion Laboratory[29]. For station TOGT, where the trajectory model cannot be robustly estimated because of the significant gap in the data, we use the best-fitting trajectory model (including the linear trend) of a nearby station TONG. This is justified because the two stations are effectively at the same location, and are only separated by 2.4 km. Similarly, for station NUE1, which has estimates of MIDAS velocities but not a robust estimate of a trajectory model, we take the average of the trajectory model parameters obtained for stations NIUM and NIUT that are 0.04 and 2.67 km from station NUE1, but use the available MIDAS velocities for the linear trends.

ICA

For obtaining a robust detection of the postseismic signal, it is crucial to disentangle it from the seasonal signals. Considering that the seasonal signals do not follow simple sinusoids and that the temporal evolution of the postseismic deformation is unknown, it is best not to prescribe any functional form for both seasonal and postseismic signals. Therefore, we utilize the ICA technique[4], which does not impose any a priori assumptions on the time evolution of these signals.

We recover five independent components that are common in all the GNSS time series, among which the second most significant component is the postseismic deformation (Fig. 1). The four other components are seasonal (or common mode) signals (Extended Data Fig. 6). The time evolutions of the seasonal components with complexities beyond simple sinusoids demonstrate the advantage of applying ICA. The most significant seasonal signal is dominant in the vertical component, whereas the second and third most significant signals are present in both the vertical and horizontal components. The significance rapidly diminishes by the fourth most significant signal. Comparison between the preprocessed time series (that is, the input for ICA) and the recovered postseismic deformation component is also shown in Extended Data Fig. 7. Note that using the data time window with a much longer time before the earthquake occurrence can dilute the postseismic signal.

Uncertainties in the detected postseismic signal

Uncertainty in the time evolution at each time step (Fig. 1b) is derived by projecting the uncertainties in the original GNSS time series through ICA. For estimating the uncertainties in the cumulative displacements of postseismic deformation (Fig. 1a), we use the GNSS stations in New Caledonia. Considering these stations are far from the earthquake and close to each other, postseismic displacements at these locations are predicted to be nearly uniform. Therefore, we take the standard deviation of each of the three-component displacements as the uncertainty for each component.

Modelling viscoelastic relaxation

We use a semianalytical Fourier-domain solver, Relax[5,6], to model the viscoelastic relaxation. Our computational domain is defined by $512 \times 512 \times 512$ grids with 8 km grid spacing, where the seismic source is located at the centre. For the source, six finite sources derived from the multi-point source solutions[18] are used to accurately represent the source mechanism (Extended Data Table 2). Various layers are included in the viscosity structure: three layers that are common to all models, that is, the elastic lithosphere (0–80 km), viscoelastic upper (80–670 km) and lower (greater than 670 km) mantle and a weak layer with variable depth and thickness. The asthenosphere and the MTZ correspond to depth ranges of 80–220 km and 410–670 km, respectively. Maxwell rheology is assumed, and each layer has a Maxwell time (and a corresponding viscosity value associated with it: 41.7 and 833.3 years for the upper and lower mantle, respectively). The elastic slab structure is also included in most models, which closely follows the geometry of the Tonga slab[23,27] and encloses the earthquake source (Extended Data Table 2). The modelling is performed for a flat Earth, and we set the locations of the trench and GNSS stations such that the great-circle distance and azimuth with respect to the earthquake centroid location are preserved. Note that the flat-Earth assumption results in an underestimation of the surface deformation because of the larger hypocentral distance for a given epicentral distance than for a spherical Earth. However, the increase in the hypocentral distance is less than 3% within the 500 km epicentral distance and less than 5% within the 2,000 km epicentral distance, producing insignificant effects compared to the uncertainties in the estimated postseismic displacements.

Our modelling approach allows for a 3D viscosity structure as expected in the subduction setting, which is crucial for correctly predicting the surface deformation (Fig. 2). However, it restricts the elastic structure to be a homogeneous half space. We select values that are close to the average elastic structure throughout the upper mantle, bulk and shear moduli of 12.88×10^4 MPa and 7.73×10^4 MPa ($= \mu_{\mathrm{ref}}$), respectively, which correspond to the mantle elasticity at about 300 km depth (Extended Data Fig. 8). This half-space elastic structure should be considered for the conversion between the Maxwell time and the viscosity. We input a certain Maxwell time ($\eta/\mu = \eta_{\mathrm{ref}}/\mu_{\mathrm{ref}}$) for each viscoelastic layer for the modelling, which corresponds to a viscosity value (η_{ref}) for the given constant shear modulus (μ_{ref}). Because the modulus (μ) varies with depth, the corresponding viscosity value (η) for a given Maxwell time would also vary, such that the viscosity and the shear modulus would scale with each other. Therefore, we calculate viscosity as $\eta = \eta_{\mathrm{ref}}\mu/\mu_{\mathrm{ref}}$, which is μ times the corresponding Maxwell time. The variation of the shear modulus, however, is less than a factor of two in the upper mantle, about 0.8 to 1.6 times the constant reference value (μ_{ref}) in the depth range of 80 km (bottom of the elastic lithosphere) to 670 km (Extended Data Fig. 8). This leads to variation in the corresponding viscosity values of less than a factor of two, which is not as significant as the orders of magnitude differences in viscosity in the layers considered in the modelling.

The modelling produces a three-component displacement time series for all grid points on the surface (Fig. 2). Among these, we extract the time series at the GNSS station locations used in this study and apply the same ICA to these time series. This results in a common time evolution and cumulative displacements, that is, spatial pattern, to be compared with the observed postseismic deformation (Figs. 3 and 4 and Extended Data Fig. 7). Note that the ICA for the modelled time series results in a single dominant independent component, which is the postseismic deformation.

Coseismic displacements

We also obtain estimates for the coseismic displacements from the earthquake (Extended Data Fig. 1) through the trajectory model fitting process[30] performed before the ICA. The observed displacements can be compared with the predictions made by the modelling process by using the half-space elastic structure (Modelling viscoelastic relaxation). Note that the half-space modelling with an average elastic

structure, which is commonly used for studies of shallow earthquakes, also provides sufficiently accurate coseismic displacements for deep earthquakes[31,32].

Both observed and predicted displacements are largely compatible with each other with some discrepancies. The differences are probably attributed to the Earth's curvature that is not taken into account in the flat-Earth modelling and the complexity in the earthquake mechanisms that is not captured by the six-subevent representation of the source. These factors are present in postseismic deformation modelling as well, and we, therefore, expect a similar level of discrepancies between the observed and predicted postseismic deformation as in Fig. 4a.

Evaluation of fit to the data

We evaluate two measures of fit: one for the cumulative displacements and the other for the time evolution. By doing so, we can effectively separate and examine the roles of the weak zone location and the viscosity. For both the displacements and the time evolution, we measure the χ^2 misfit, $\chi^2 = \frac{\sum_{i=1}^{n} w_i (m_i - d_i)^2 / \sigma_i^2}{\sum_{i=1}^{n} w_i}$, where m_i and d_i are modelled and data values, respectively, for the ith displacement or the ith value of the time evolution out of the total number of data values n, and σ_i and w_i are the data uncertainty and the weight associated with them. The weight is applied to account for the non-uniform spatial distribution of the GNSS stations, such that $w_i = 1/N$, where N is the number of stations within 3° including the station itself.

Data availability

GNSS data were obtained from the Nevada Geodetic Lab (geodesy.unr.edu). We also provide the detected postseismic signal, for example, displacements and time evolution, as source data for Fig. 1. Source data are provided with this paper.

Code availability

The forward modelling code RELAX is available at https://geodynamics.org/cig/software/relax/. The code for the ICA has been made available[33] on the Zenodo repository, https://doi.org/10.5281/zenodo.4322548.

28. Blewitt, G., Kreemer, C., Hammond, W. C. & Gazeaux, J. MIDAS robust trend estimator for accurate GPS station velocities without step detection. *J. Geophys. Res. Solid Earth* **121**, 2054–2068 (2016).
29. SONEL. GPS TONGA. https://www.sonel.org/spip.php?page=gps&idStation=894 (2022).
30. Bevis, M. & Brown, A. Trajectory models and reference frames for crustal motion geodesy. *J. Geod.* **88**, 283–311 (2014).
31. Jiao, W., Wallace, T. C., Beck, S. L., Silver, P. G. & Zandt, G. Evidence for static displacements from the June 9, 1994 Deep Bolivian Earthquake. *Geophys. Res. Lett.* **22**, 2285–2288 (1995).
32. Vidale, J. E., Goes, S. & Richards, P. G. Near-field deformation seen on distant broadband seismograms. *Geophys. Res. Lett.* **22**, 1–4 (1995).
33. Gualandi, A. & Liu, Z. Variational bayesian independent component analysis for InSAR displacement time-series with application to central California, USA.*J. Geophys. Res. Solid Earth* **126**, (2021).
34. Dziewonski, A. M. & Anderson, D. L. Preliminary reference Earth model. *Phys. Earth Planet. Inter.* **25**, 297–356 (1981).

Acknowledgements We thank M. Gurnis, H. Kanamori and R. Bürgmann for useful discussions. This work was partially support by the National Science Foundation grant NSF EAR 2142152.

Author contributions S.P. conceived the study, analysed the data, performed the modelling, interpreted the results and wrote the manuscript. J.-P.A. supervised the ICA and modelling and participated in the interpretation. Z.Z. participated in the interpretation. A.G. provided the code for the ICA and guided the time series analysis. All authors discussed the results and commented on the manuscript.

Competing interests The authors declare no competing interests.

Additional information
Supplementary information The online version contains supplementary material available at https://doi.org/10.1038/s41586-022-05689-8.

Correspondence and requests for materials should be addressed to Sunyoung Park.

Peer review information *Nature* thanks Yuri Fialko and the other, anonymous, reviewer(s) for their contribution to the peer review of this work. Peer reviewer reports are available.

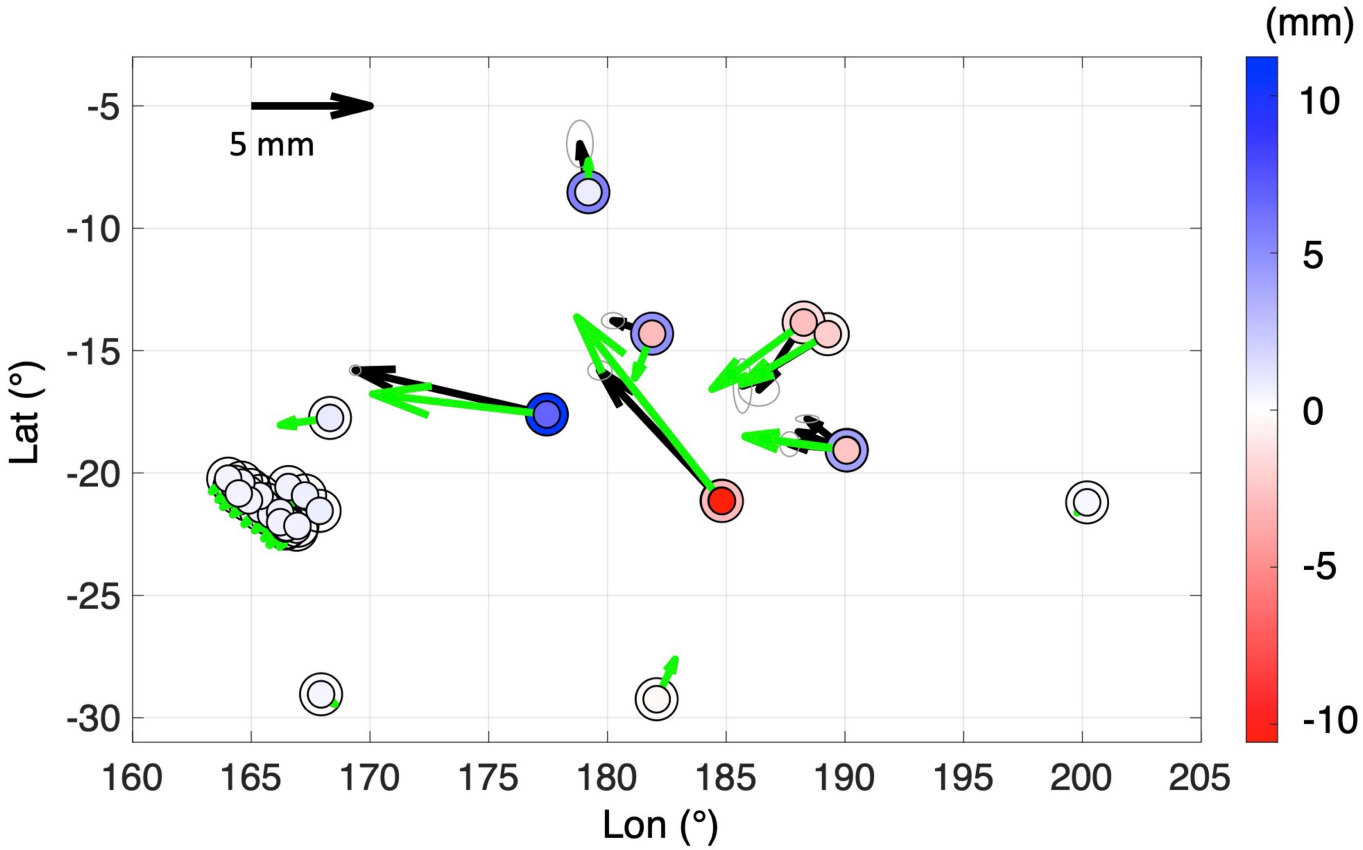

Extended Data Fig. 1 | Observed (black arrows, large circles) and predicted (green arrows, small circles) coseismic deformation. Same as Fig. 4a, except coseismic displacements are plotted. Error ellipses (grey circles; 95% confidence intervals) are obtained from trajectory modelling.

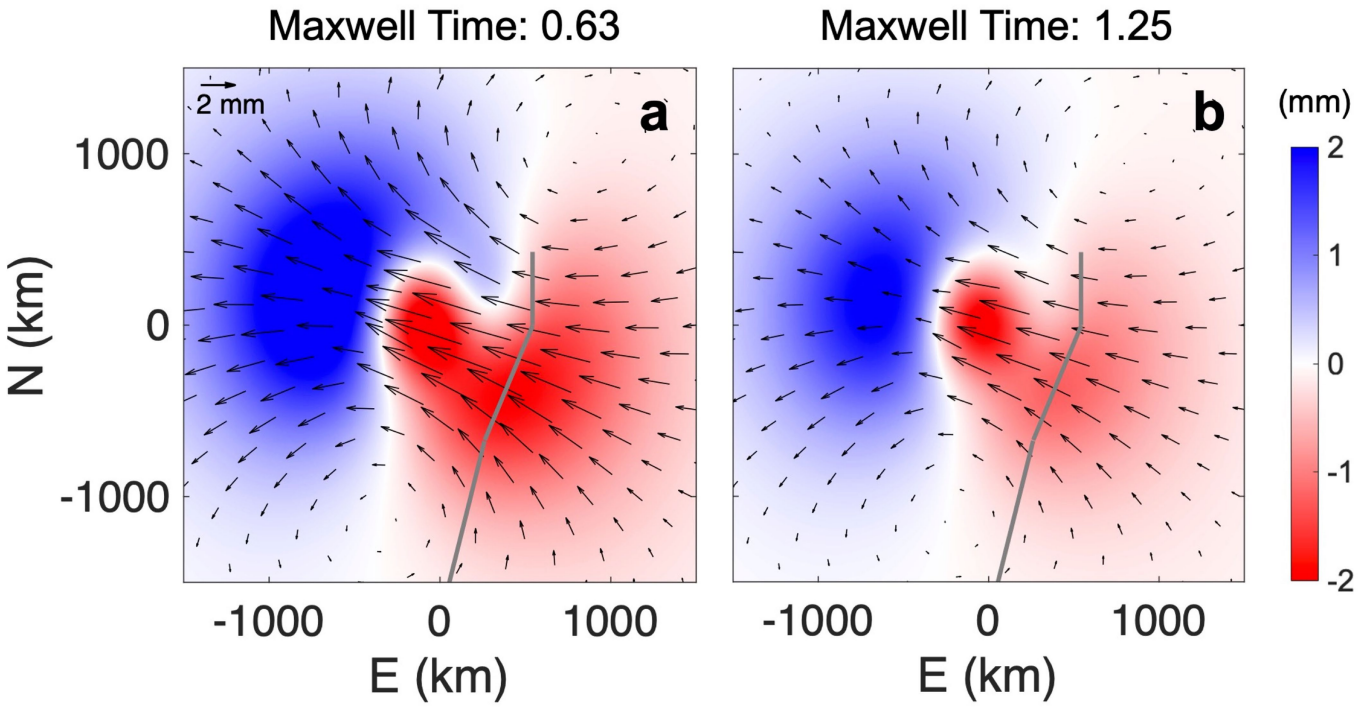

Extended Data Fig. 2 | Predicted postseismic deformation for weak MTZ BH with two different Maxwell times. a, The same as the right panel of Fig. 2f. **b**, The same as **a**, but with weak MTZ BH (Maxwell time of 1.25 years).

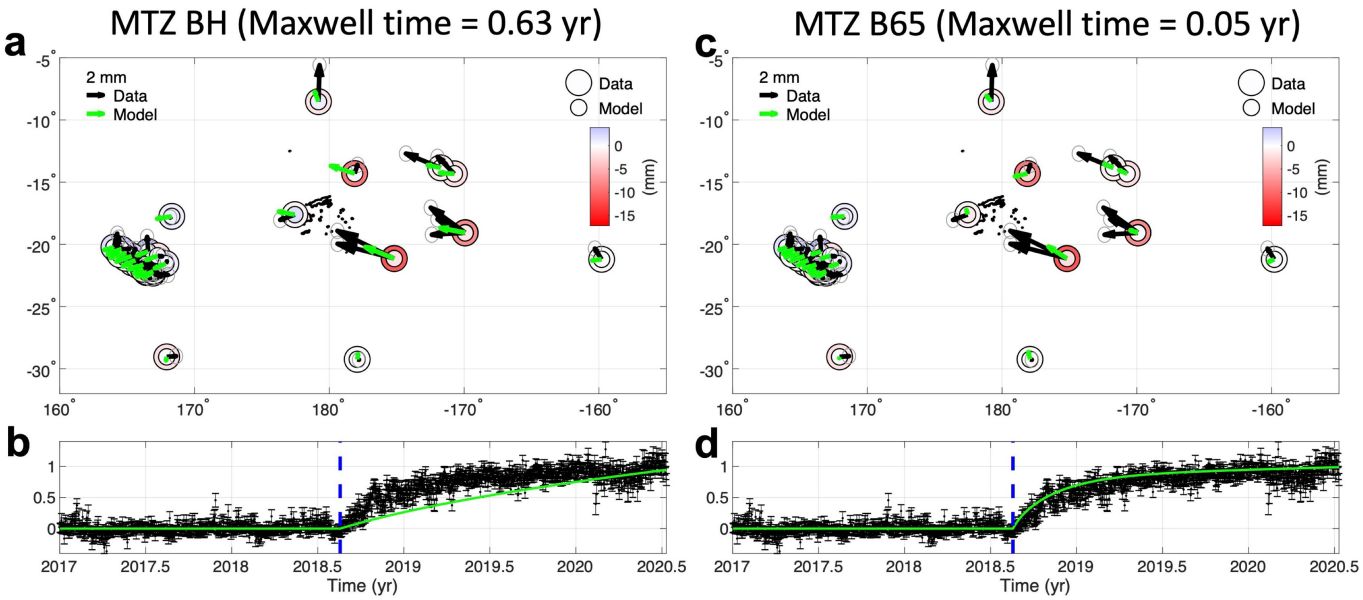

Extended Data Fig. 3 | Postseismic deformation predicted by different models (MTZ BH with 0.63-year Maxwell time and MTZ B65 with 0.05-year Maxwell time) compared against the data. a–**b**, The same as the Fig. 4a,b but with increased viscosity MTZ BH of 0.63-year Maxwell time. **c**–**d**, The same as **a**–**b**, except with reduced viscosity MTZ B65 of 0.05-year Maxwell time.

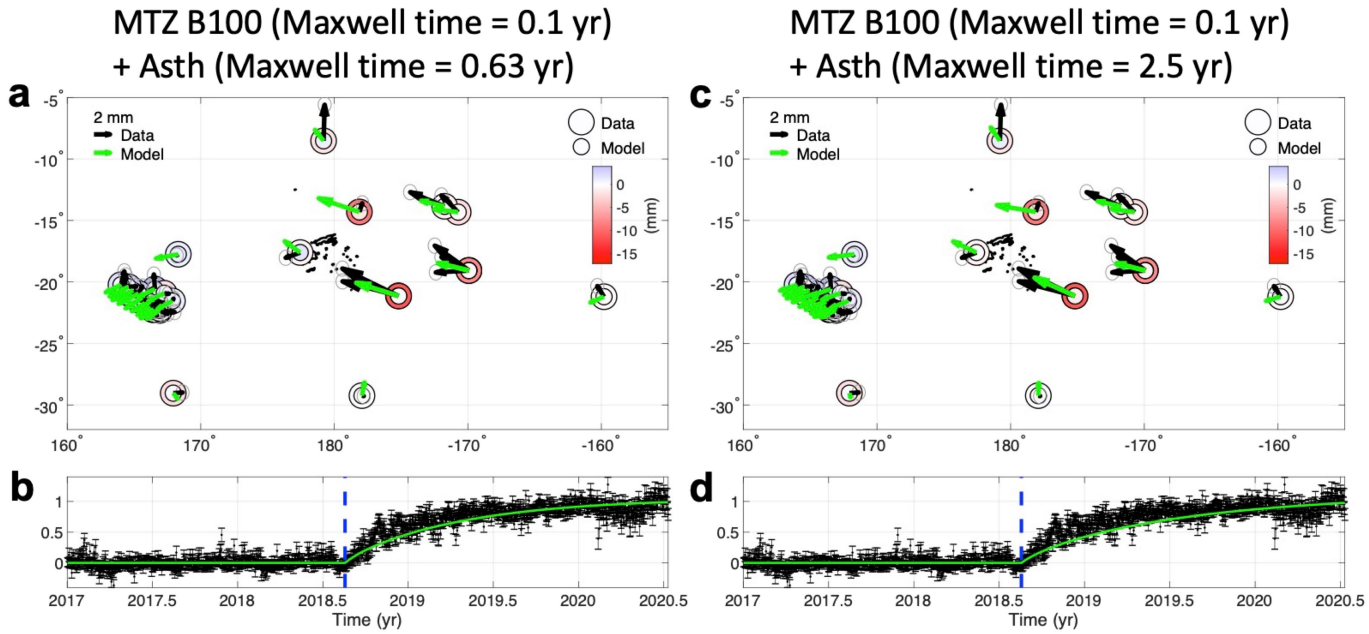

Extended Data Fig. 4 | Postseismic deformation predicted by our preferred model in presence of a weak asthenosphere. a–**b**, The same as the Fig. 4a,b but with a weak asthenosphere of 0.63-year Maxwell time. **c**–**d**, The same as **a**–**b**, but with a weak asthenosphere of 2.5-year Maxwell time. In each case, the displacements are close to the linear summation of the displacements resulting from modeling the weak asthenosphere and the weak base of MTZ separately. Horizontal displacements are in similar directions, and add constructively, resulting in 10 to 20 % larger displacements at the sites close to the earthquake. On the other hand, due to the uplift in the west of the epicentre and west of the trench produced by the weak asthenosphere, opposite from those produced by weak base of MTZ (Fig. 2), the vertical displacements tend to add destructively in stations in Fiji and Tonga islands (such as LAUT and TONG). This decreases (worsens) the overall fit to the observation by about 14 and 6 %. These results suggest that, in order to explain the observed subsidence around the epicenter and the trench in presence of weak asthenosphere, the weak zone at the base of MTZ is even more strongly required.

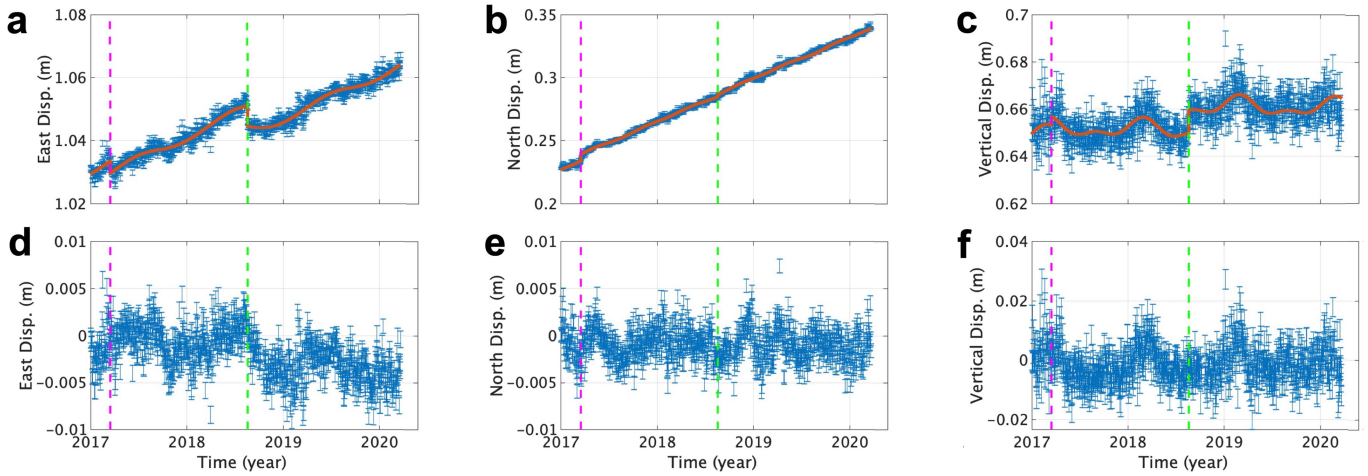

Extended Data Fig. 5 | Raw and pre-processed GNSS data of station LAUT. **a**–**c**, Raw GNSS data of east, north, and vertical components with uncertainties (blue error bars; one standard deviation). Magenta and green dashed lines denote the timings of steps associated with instrument issues and coseismic displacements, respectively. Solid orange line represents the best-fitting trajectory model. **d**–**f**, The same as **a**–**c**, except for the timeseries are pre-processed, i.e., linear trend and offsets derived from the trajectory model removed from raw data (**a**–**c**).

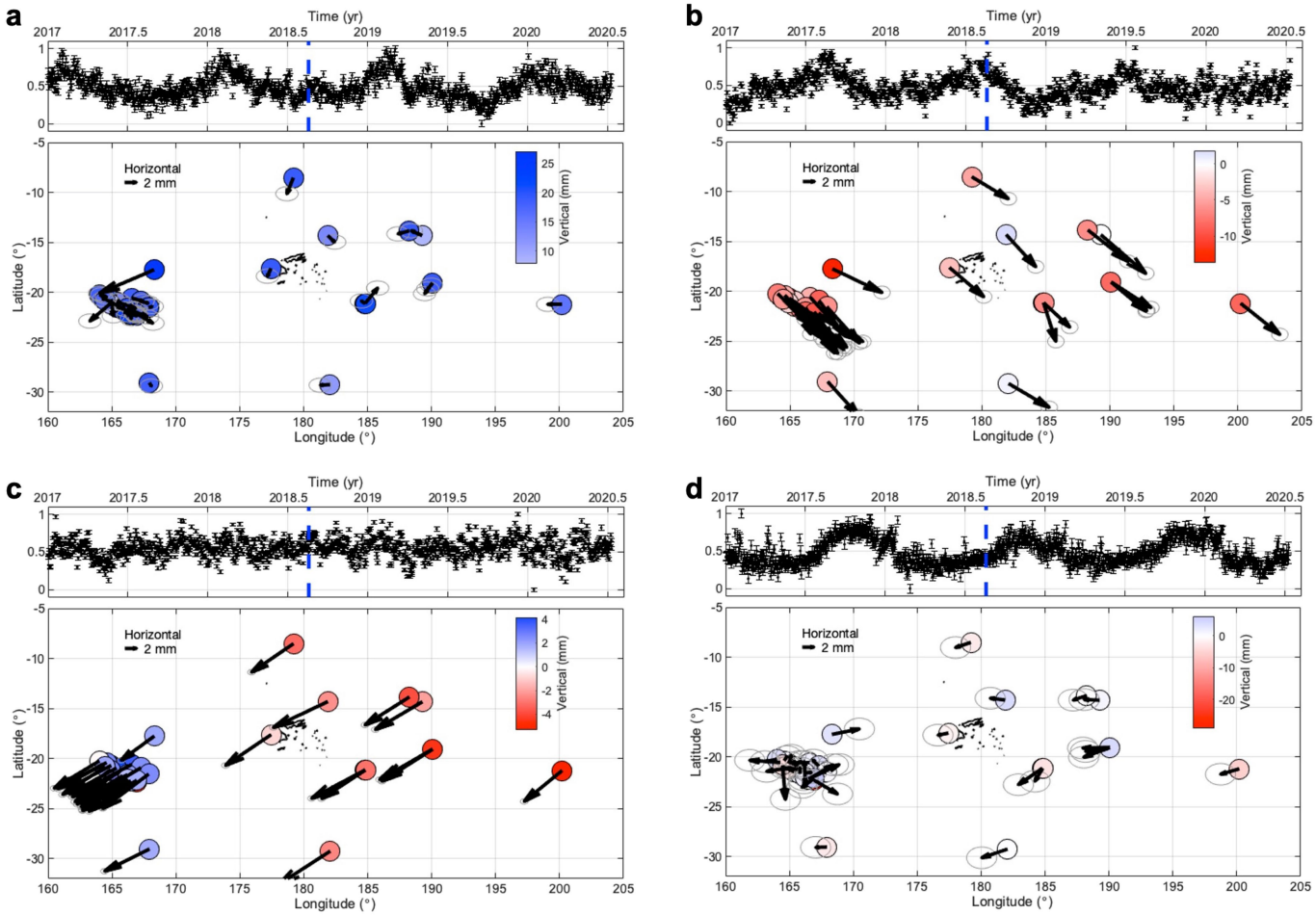

Extended Data Fig. 6 | Independent components other than the postseismic component, and their spatial distributions. a, The time evolution (top) and the spatial distribution of the most significant seasonal deformation component, shown in the same manner as in Fig. 1, where error ellipses (one standard deviation) are estimated in the same way as those of postseismic displacements. **b**–**d**, The same as **a**, but for the 2nd, 3rd, and 4th most significant seasonal components, respectively.

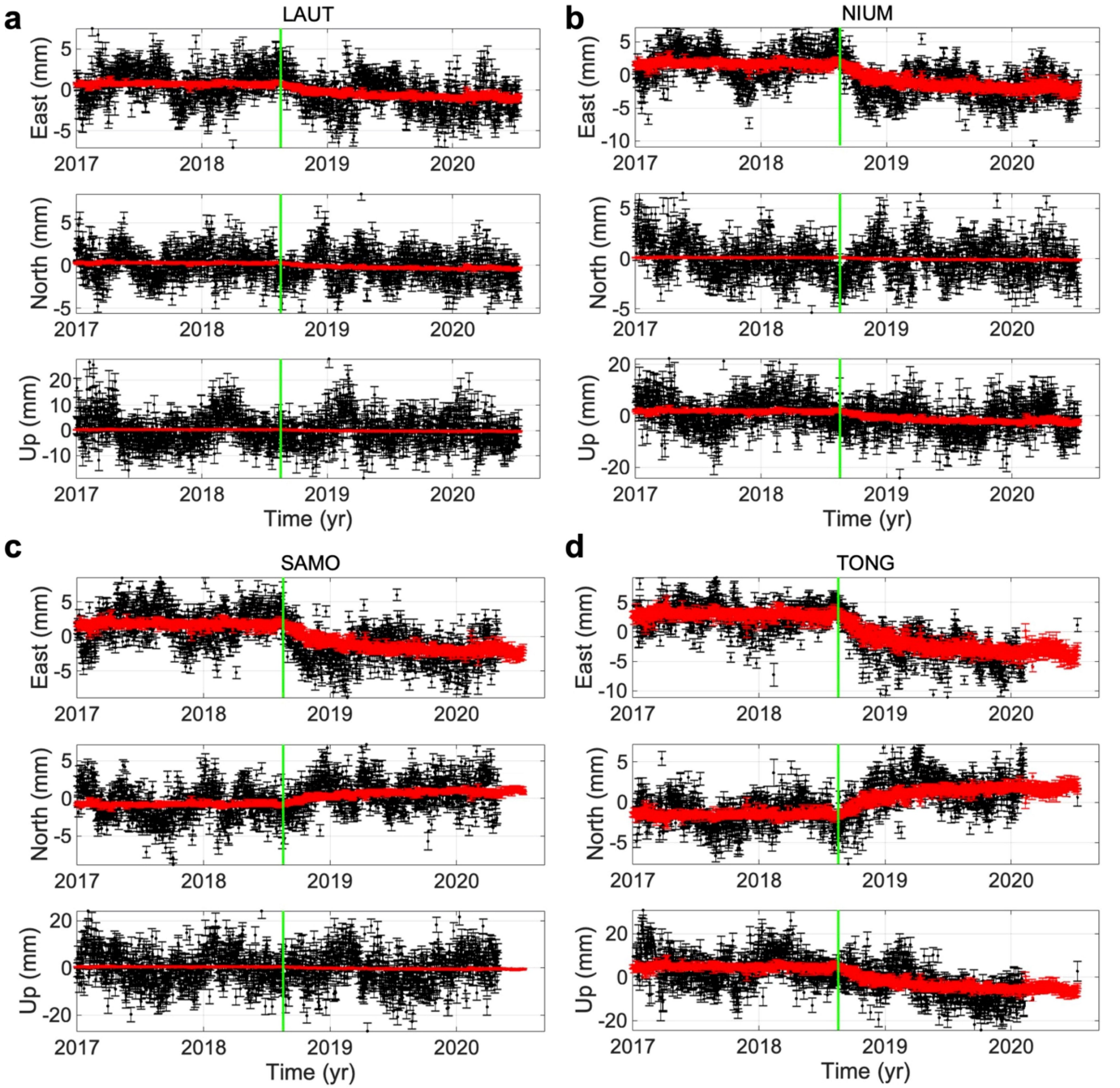

Extended Data Fig. 7 | Postseismic deformation at each pre-processed GNSS timeseries. a, Pre-processed east (top), north (middle), and up (bottom) components of the GNSS data of station LAUT (the same as Extended Data Fig. 5d–f) are plotted in black, while the contribution from the postseismic deformation in each timeseries is plotted in red. Error bars are for one standard deviation. The time of the earthquake is shown with a solid green line. Note that the scale of up component is larger than those of horizontal components. **b**–**d**, Same as **a**, but for stations NIUM, SAMO, and TONG, respectively. Stations SAMO and TONG have gaps in data close to the end of the analyzed time period.

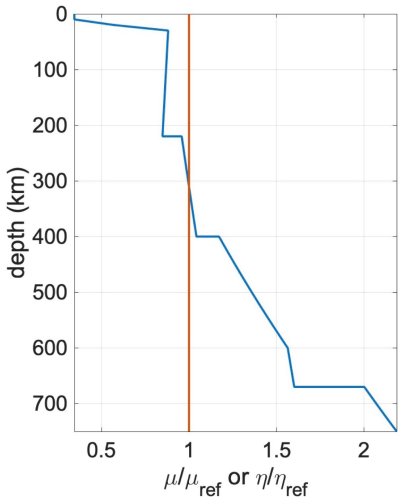

Extended Data Fig. 8 | Ratio of the shear modulus (μ) and viscosity (η) to the reference values (μ_{ref}, η_{ref}) as a function of depth. The ratios (solid blue line) with respect to the reference (solid orange line) are calculated based on the Preliminary Reference Earth Model[34].

Extended Data Table 1 | GNSS stations used in this study

Station Name	Longitude (°)	Latitude (°)
ASPA	-170.722433	-14.326097
CKIS	-159.800609	-21.201028
FTNA	-178.120943	-14.307805
GOR3	166.905005	-22.314989
HGHN	164.943054	-20.688837
HLOB	165.627285	-21.276863
IAAI	166.565806	-20.574768
KOUC	164.287336	-20.558693
LAUT	177.446580	-17.608815
LCAP	165.375477	-21.480344
LFOA	165.831616	-21.709372
LPIL	167.263781	-20.917987
MRTG	167.875795	-21.547559
NBTG	166.41612	-22.241995
NIUM	-169.927066	-19.076528
NIUT	-169.920652	-19.052998
NMEA	166.442516	-22.264788
NORF	167.938832	-29.043346
NRMD	166.484885	-22.228326
NRMG	166.484886	-22.228323
NUE1	-169.927230	-19.076175
PDME	165.351321	-20.937880
PEBO	164.581000	-20.392487
PMBT	164.901369	-21.118626
POUE	164.023827	-20.231343
PTVL	168.315024	-17.749433
RAUL	-177.928950	-29.244665
SAMO	-171.738419	-13.849212
THIO	166.215372	-21.608582
TOGT	-175.196770	-21.130263
TONG	-175.179225	-21.144713
TTTA	166.216891	-22.011517
TUVA	179.196562	-8.525292
UACO	164.469922	-20.836282
YATE	166.944372	-22.159549

Extended Data Table 2 | Input source and slab geometry for modeling

Earthquake source (6 subevents)									
no.	slip (km)	x_s (km)	y_s (km)	z_s (km)	length (km)	width (km)	strike (°)	dip (°)	rake (°)
1	2.13E-03	-1.77E+01	-5.15E+01	5.50E+02	4.00E+01	4.00E+01	64.8	89.8	-71.2
2	3.19E-03	-1.82E+01	-2.12E+01	5.50E+02	4.00E+01	4.00E+01	25.5	76.6	-81.7
3	2.68E-03	6.74E+00	-5.05E+01	5.51E+02	4.00E+01	4.00E+01	150.5	14.2	-157.1
4	5.26E-03	-6.53E+00	-1.75E+01	5.43E+02	4.00E+01	4.00E+01	7.0	68.2	-90.7
5	3.93E-03	-4.26E+00	-3.11E+01	5.35E+02	4.00E+01	4.00E+01	10.0	67.5	-103.3
6	5.62E-03	6.36E+01	-3.62E+01	5.36E+02	4.00E+01	4.00E+01	228.9	19.7	-38.6

Slab geometry (defined using 3 rectangular prisms)								
no.	x_1 (km)	x_2 (km)	x_3 (km)	length (km)	width (km)	thickness (km)	strike (°)	dip (°)
1	-1.40E+1	5.75E+2	4.00E+1	7.27E+2	1.00E+3	1.00E+2	202.8	41.9
2	4.27E+2	5.75E+2	4.00E+1	4.27E+2	1.00E+3	1.00E+2	180.0	41.9
3	-6.84E+2	2.93E+2	4.00E+1	1.26E+3	1.00E+3	1.00E+2	194.0	41.9

Each of the six subevents[18] is characterized by slip on a fault with the top tip coordinate (north, x_s; east, y_s; depth, z_s), along-strike length, width in the down-dip direction, strike, dip, and rake angles. Note that the origin is the centroid location. The slab is defined by 3 rectangular prisms, each described by the position of the tip of the central plane (north, x_1; east, x_2; depth, x_3), along-strike length, width in the dip direction, strike, and dip angles. These parameterizations are consistent with the input format of the Relax software.